



PERGAMON

Continental Shelf Research 22 (2002) 1565–1578

CONTINENTAL SHELF
RESEARCH

www.elsevier.com/locate/csr

Direct stress measurements in a shallow, sinuous estuary

Harvey E. Seim^{a,*}, Jackson O. Blanton^b, Thomas Gross^c

^a *Dept. of Marine Sciences, University of North Carolina at Chapel Hill, Chapel Hill, NC, USA*

^b *Skidaway Institute of Oceanography, Savannah, GA, USA*

^c *National Ocean Service, NOAA, Silver Springs, MD, USA*

Received 25 June 2001; accepted 14 September 2001

Abstract

Observations from a 4 element mooring array collected in a bend of a shallow, sinuous estuary are used to describe the flow, density structure and momentum balance over a 10-day period. In general, the flow in the lower 3 m is stratified on ebb and unstratified on flood and shear is concentrated near the bed on flood and nearly uniform throughout the water column on ebb. At spring tides stratification is reduced and the flows 1 m above bottom (mab) are consistently greatest at the downstream end of the bend. The along-channel density gradient is weakest during spring tides owing to zero gradient over most of ebb flow. At neap tides vertical stratification is strong enough to raise the gradient Richardson number well above 0.25 for most of the ebb tide. Currents are weaker and do not display a regular along-channel pattern. The variation in density and current structure is interpreted to result from variations in cross-channel circulation associated with the channel bend. At spring tides, the cross-channel circulation appears to be strong enough to overturn the water column whereas at neap tides stratification is strong enough to halt the overturning.

Reynolds stress measured with a Benthic Acoustic Stress Sensor undergoes a four-fold increase between neap and spring tide. The drag coefficient relative to flow at 1 mab is 0.0015–0.0025. Bed stress in the bend is estimated using this drag coefficient and the maximum instantaneous velocity at 1 mab over the array. Because of the along-channel variability in current speed, the estimated bed stress is roughly twice as large as the measured Reynolds stress in the middle of the bend. The estimated bed stress is found to balance the horizontal pressure gradient and local acceleration, implying that a depth-averaged linear momentum balance adequately describes the dynamics on the bend when the impact of the cross-channel circulation is taken into account in the estimate of the bottom stress. © 2002 Elsevier Science Ltd. All rights reserved.

Keywords: USA; Georgia; Satilla River; Estuary; Circulation; Momentum balance

1. Introduction

Despite the acknowledged importance of turbulent mixing of momentum and density in estuaries (e.g. Hansen and Rattray, 1965; Geyer et al.,

2000), there have been relatively few direct observations of turbulence in estuaries. Trowbridge et al. (1999) and Peters (1999) report some of the first comprehensive turbulence observations collected in the context of the larger scale flow, from the Hudson River. Turbulent mixing is found to be of first-order importance in the momentum and salt balances. Except for salt-wedge estuaries where stratification is presumed to be strong

*Corresponding author. Tel.: +1 919 962 2083 fax: + 1 919 962 1254.

E-mail address: harvey_seim@unc.edu (H.E. Seim).

enough to completely suppress upward stirring of bottom-generated turbulence, bottom friction generated by tidal currents is often the principal source of turbulent energy.

One of the few studies to evaluate stress measurements in light of an overall momentum balance is that of Trowbridge et al. (1999). Observations collected in the Hudson River were used to evaluate a linear momentum balance, and it was found that the bottom stress was 80% of the value required to close the momentum balance on neap tide and only 50% of the required value on spring tides. The Hudson was chosen for the study because of its particularly simple geometry. Near the ocean surface the barotropic pressure gradient and local acceleration were nearly in balance, and as the sea floor was approached bed stress became increasingly important.

Geyer et al. (2000) estimate the bottom stress as the residual of a linear momentum balance. They find this indirect stress to be consistent with a quadratic drag law, but the values are consistently greater than those measured directly by Trowbridge et al. (1999) and water column dissipation measurements collected at the same time by Peters

and Bokhorst (2000). The implication is that some process not captured by the direct measurements of turbulence contributes significantly to stress production. They suggest spatial structure in the bottom stress field and/or secondary circulation as candidate mechanisms.

This study concerns the Satilla River which lies in the coastal plain of Georgia and is characterized by a series of relatively sharp channel bends in the lower 25 km of the estuary (Fig. 1). An extensive saltmarsh surrounds the estuarine system and the intertidal region accounts for roughly 70% of the total area. The system experiences 0.75–1.5 m amplitude semi-diurnal tides, which produce 0.5–1 m s⁻¹ amplitude depth-averaged tidal currents. The 4–10 m deep main channel follows a sinuous path and salt can intrude in excess of 40 km inland. In the lower 25 km of the estuary the main trunk is relatively broad (O(1 km)) and often exhibits a primary and secondary channel. Freshwater inflow to the Satilla is typically small, averaging 70 m³ s⁻¹, but occasionally rises to in excess of 150 m³ s⁻¹ or falls to nearly zero. Vertical stratification is typically weak at spring tides (<2 kg m⁻³ change in density

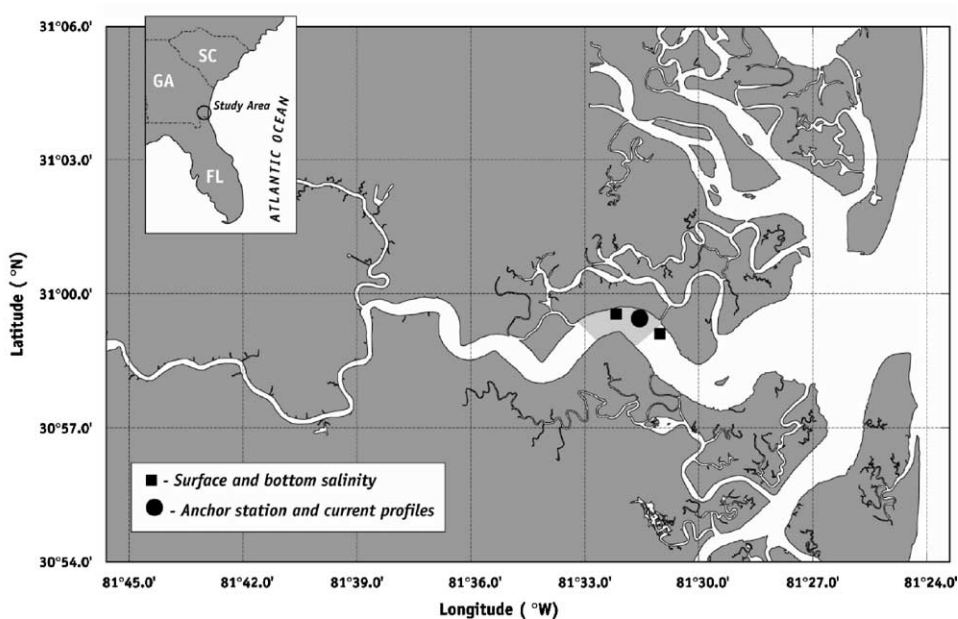


Fig. 1. Low water outline of the Satilla River. Moorings were located in the shaded region.

top-to-bottom) and stronger during neap tides ($<5 \text{ kg m}^{-3}$ change in density top-to-bottom) and is dominated by salinity variations. Tides are weakly ebb-dominant in the main channel but overtide amplitudes grow rapidly in the tidal creeks off the main channel (Blanton et al., 2002). Slack water lags mean high water and mean low water by about 1 h (Blanton et al., 2002).

In this paper, we examine the flow structure on a fairly sharp bend in the Satilla River (radius of curvature of roughly 1500 m) with a small mooring array. Our interpretation of the results is that secondary circulation associated with flow curvature strongly influences the velocity and density field. Near-bottom currents at spring tide are greatest at the downstream end of the bend, consistent with secondary circulation carrying high momentum, near-surface flow to the bottom. We estimate the bed stress on the bend from the maximum near-bed velocity, finding that this roughly doubles the Reynold's stress directly observed near the middle of the bend. A depth-averaged linear momentum balance adequately represents the along-channel dynamics when the bottom-stress estimate is used.

This article is organized as follows. We first describe the mooring system used in this study, then present the results. After introducing the horizontal density and current variations, the vertical structure and stress measurements are presented, and the drag coefficient is estimated. The focus of the paper is evaluation of the momentum balance, testing whether a linear balance is satisfied in this system, and if so, under what conditions. A brief discussion follows.

2. Methods

A mooring array deployed in a bend of the Satilla River, Ga, from late March to late April 1997 is used to examine the structure of the bottom boundary layer (Fig. 2). The array consisted of three moorings sites separated by approximately 1.5 km along the channel. The upstream (to the west, designated W) and downstream (to the east, designated E) moorings measured pressure, salinity, temperature with

Seabird Seacats and optical backscatter at 0.66 and 2.5 m above the bottom mab. Currents were measured with an InterOceans S4 at 1 mab. At the central mooring (designated C) turbulent velocities were measured with the Benthic Acoustic Stress Sensor (BASS, Williams et al., 1987) at 0.28, 0.66, 0.98 and 1.33 mab (pods 1, 2, 3, and 4, respectively) and pressure, salinity, temperature and optical backscatter were measured at 0.66 and 2.5 mab with Seacats. The Seacats recorded measurements every 6 min, and BASS collected 4.5 min bursts of 2 Hz data every 10 min. An upward-looking 600 kHz broadband acoustic Doppler current profiler (ADCP) was deployed roughly 100 m from the BASS tripod and measured averaged current velocities every 12 min at 0.5 m intervals between 2.24 mab and the sea surface. A 10-day period spanning a spring-neap cycle is examined below.

Salinity data are of excellent quality with the exception of the lower meter at E which intermittently fails. We utilize the observations but note in the graphic captions that the values are suspect. Pressure measurements from the upper sensor at E are obviously flawed, and small timing errors at the upper sensor on W and the lower sensor on C prevent their use in computing the along-channel surface slope. The optical backscatter sensors fouled after 2–3 weeks and will not be discussed in this paper.

The BASS and ADCP observations have been combined to provide as complete coverage of the water column as possible. The principal axis of the lowest ADCP measurement, 2.24 mab, was offset from the uppermost BASS tripod measurement at 1.33 mab by 12.5° , presumably owing to the separation of the instruments along the curving reach. The BASS observations were rotated to be aligned with the ADCP observations. The rotated, combined data set was then interpolated to a common time base and depth-averaged. The principal axis of the depth-averaged currents was used to define the along-channel direction. The mean and turbulent velocities were then decomposed along this axis to maintain a consistent reference frame throughout the water column. The currents from the S4 current meters were also rotated into principal

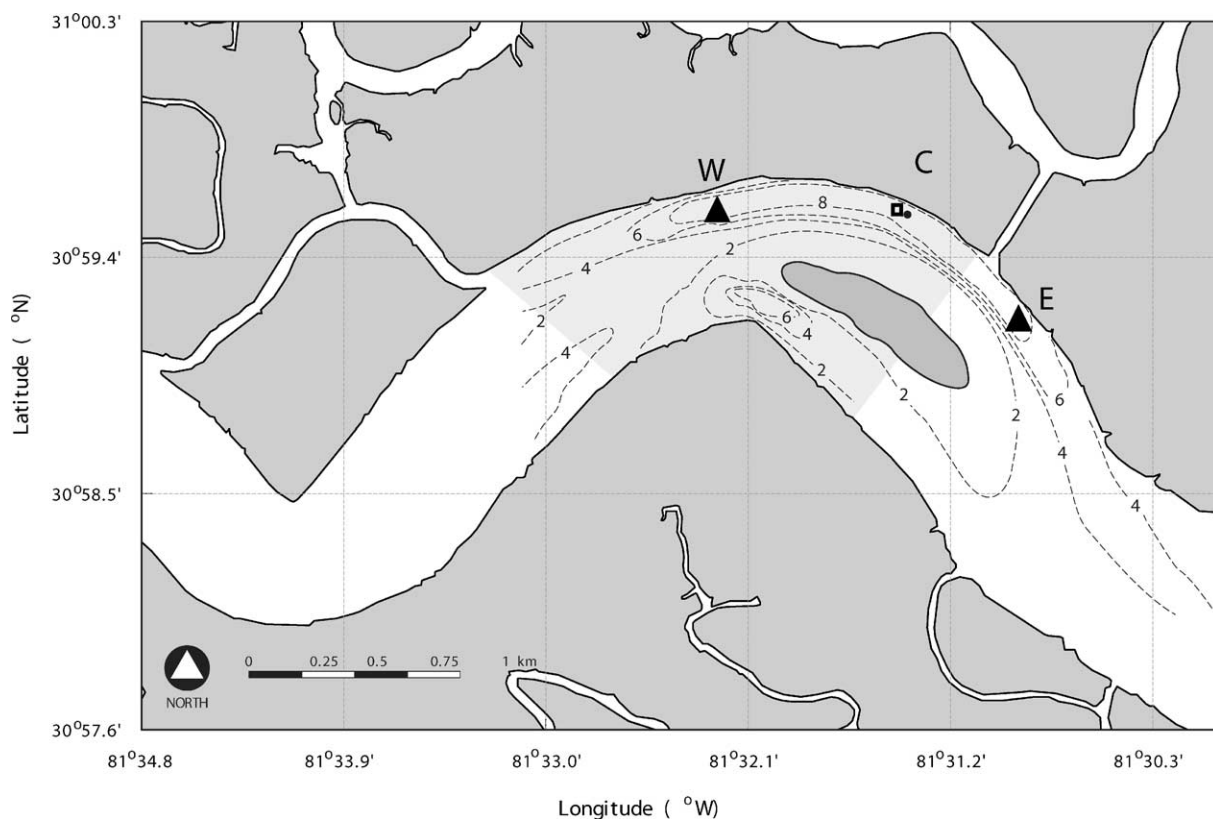


Fig. 2. Bathymetry (in meters below mean low water) of the Satilla River in the vicinity of the 1997 mooring deployment. Moorings were located in the deep channel on the outside of the bend. Triangles mark S4 and seacat deployments, the square marks the BASS, and the circle locates the upward-looking ADCP.

axes. The convention system adopted is positive seaward and northward.

The observations from BASS are of mixed quality. BASS measures currents along 4 non-orthogonal axes and (like an ADCP) therefore has more than enough information to compute a three component velocity vector. Standard procedure in processing BASS observations is to identify any of the four channels that may show only weak signals and eliminate them from further processing (i.e. the remaining three non-orthogonal components are used to compute the orthogonal velocity components). This has the advantage of allowing calculation of the stress tensor even if one of the channels is not functioning. For this deployment, pod 3 (0.98 mab) had only 3 functioning channels, and a channel on pod 4 (1.33 mab)

malfunctioned intermittently. Initial processing of the observations produced Reynolds stresses, denoted as $\langle -u'w' \rangle$, at each elevation but the results were very atypical. In particular, $\langle -u'w' \rangle$ was effectively zero on flood tide at pods 1 and 2 (0.28 and 0.66 m), and effectively zero on ebb tide at pods 3 and 4.

Reprocessing of the observations without dropping one of the four channels dramatically changed the signals. Though this significantly reduces our vertical resolution because it does not permit estimation of $\langle -u'w' \rangle$ at pods 3 and 4, the stress estimates are now comparable in the vertical and of similar amplitude during flood and ebb. We therefore use this reduced dataset (Reynolds stress from pods 1 and 2) in the rest of the study. Additional measurement issues asso-

ciated with flow blockage near BASS on flood are discussed below.

3. Results

During the mooring deployment river discharge decreased from 60 to 10 m³ s⁻¹. This was part of a larger trend of decreasing river discharge following a large flood event in late February when discharge peaked at 290 m³ s⁻¹. Salinities increased from an average of 17 on the practical salinity scale (UNESCO, 1985) in late March to 22 in late April (Fig. 3a). Tides are dominated by the 1 m amplitude M₂ tide with N₂ and S₂ each being approximately 0.2 m in amplitude. This often results in a large spring tide and small neap tide followed by a less extreme fortnightly cycle (Fig. 3b). Deployment occurred shortly after a minor spring tide (2.3 m range) followed by a moderate neap tide (1.9 m range), then a large spring tide (3 m range), a small neap tide (1.5 m range) and a minor spring tide (2.4 m). The BASS tripod fell over just before maximum spring tide on April 6 presumably because of the strong tidal currents. This study examines the conditions during the first 10 days of the deployment when

all the instrumentation was functional. To examine details of the flow, most of the graphics display several days of data from the first neap tide and just before the maximum spring tide.

3.1. Along-channel character

Currents generally transition from maximum ebb to maximum flood very rapidly, then slow down gradually during flood for several hours before accelerating more quickly to ebb-directed flow (Figs. 4a and 5a). Currents at E and W experience a strong pulse of flood flow soon after the change in tide that is not seen at C. Salinities vary from 10 to 25 between low and high water. The increase in salinity on flood is initially rapid but slows noticeably as flood currents decelerate, presumably at the same time that the water begins to flood the marsh (Figs. 4b, c and 5b, c).

A reasonably consistent horizontal salinity gradient is maintained during flood, but it is of more varied character on ebb. On average the horizontal salinity gradient is 1.1 psu km⁻¹ over

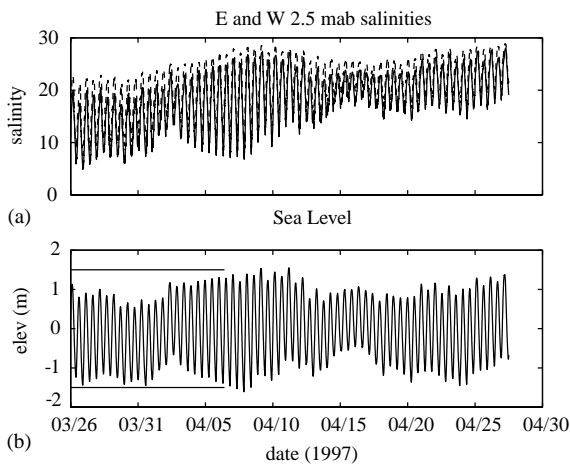


Fig. 3. (a) Salinities from the east (dashed line) and west (solid line) moorings and (b) pressure at the central mooring during the deployment period. The horizontal lines on the pressure record mark the time when the BASS tripod was working.

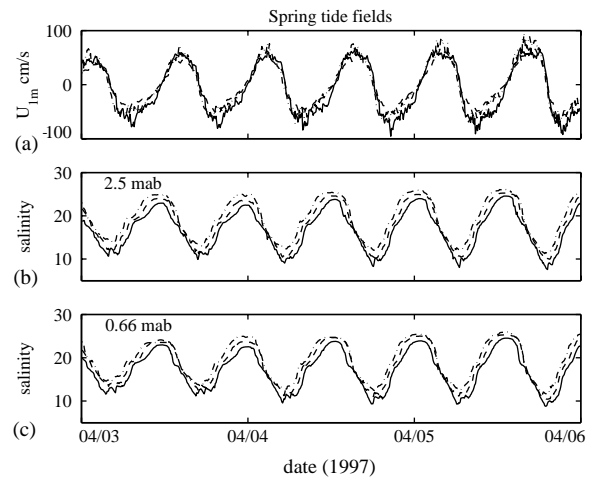


Fig. 4. Times series at spring tide of (a) along-channel currents 1 mab (b) salinity 2.5 mab and (c) salinity 0.66 mab from the west (W, solid), central (C, dashed) and east (E, dash-dot) moorings. Ebb currents are positive. Note that currents are maximum at E on ebb and maximum at W on flood. The along-channel salinity gradient goes to zero during part of ebb but is maintained on flood. The salinity sensor at 0.66 mab at E was intermittently malfunctioning.

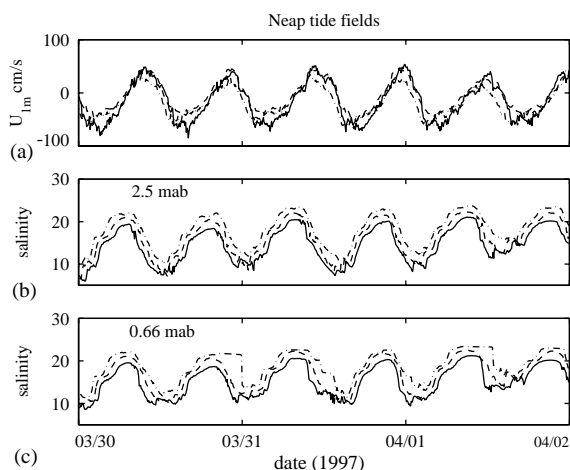


Fig. 5. Times series at neap tide. Labeling as in Fig. 4. Note that currents at E are weak on ebb and reverse nearly 1 h earlier than at C or W. The along-channel salinity gradient is remarkably constant over the tidal cycle. The salinity sensor at 0.66 mab at E was intermittently malfunctioning.

the array. During spring tides the gradients are 10–20% smaller, and on ebb gradients collapse to zero, first in the east half of the array, later in the western half, at both 0.66 and 2.5 mab (Figs. 4b and c). A rapid decrease in salinity at E soon after ebb begins this process. Wave-like fluctuations in salinity characterize low water and can lead to short-term reversals in the sign of the salinity gradient. During flood, currents are regularly greatest at W, whereas on ebb, currents tend to be greatest at E. At C the currents follow the slower of the two flows, and the general pattern that emerges is that currents 1 mab are greatest at the mooring farthest downstream with respect to the instantaneous flow direction (Fig. 4a).

On neap tides, the average horizontal salinity gradient is 1.2 to 1.3 psu km^{-1} . The gradient is maintained on ebb but now the strongest gradients on ebb are established between C and E near low water (Figs. 5b and c). This occurs when currents at E reverse roughly an hour in advance of those at C and W. The wave-like salinity fluctuations at low tide are stronger and more persistent than during spring tides. Currents at E are 10–20 cm s^{-1} weaker on ebb than at C and W, and currents at W are 10–20 cm s^{-1} stronger on

flood than at C and E. At C the currents follow those at E on flood and those at W on ebb.

Currents at C are systematically smaller than those at E and W on flood, and in particular fail to achieve the maximum (negative) values observed early on flood (Figs. 4a and 5a). This suggests a local flow disturbance near C that may be influencing its measurements at 1 mab. Further evidence supporting this supposition is presented below.

3.2. Vertical structure

Mean horizontal currents as a function of height above the bottom at C over the 10-day period reveal a classic estuarine circulation of inflow near the bed and outflow above mid-depth (Fig. 6a). Area-weighted averaging (Kjerfve and Seim, 1984) was used to form the vertical profiles. These profiles differ from the Eulerian average velocities by roughly a 2 cm s^{-1} landward velocity, which is an estimate of the Stokes drift owing to the tide (Cheng, 1988). At 1 mab current means at E and W are also shown, and it is obvious that C is biased toward zero.

The average along-channel velocity profile on ebb (Fig. 6b) is fairly uniformly sheared in the vertical, whereas the average along-channel flood profile is strongly sheared near the bed and weakly sheared higher in the water column. This is consistent with the interaction of the mean estuarine circulation with the tide (Jay and Smith, 1990). Comparison of average flood values at E, C and W confirms the bias towards zero on flood at C.

In the average cross-channel velocity profile (Fig. 6c) on flood there is flow toward the outside of the bend above 2.5 mab and flow toward the inside of the bend below this elevation. The vertical structure is consistent with flow induced by a channel bend in unstratified fluid. On ebb there is flow toward the outside of the bend above 7 m and near the bottom, and flow towards the inside of the bend at mid-depth. The mid-depth flow is trapped closer to the surface during neap tides and penetrates closer to the bed during spring tides but the three-layer structure is maintained.

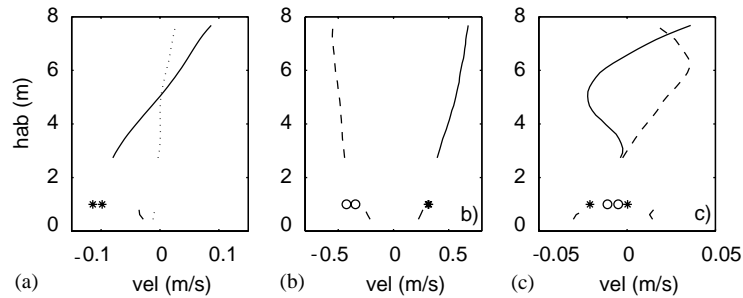


Fig. 6. (a) Average along-channel velocity profile at C. Asterisks show values at moorings E and W. Inflow of up to 10 cm s^{-1} occurs below 4.5 mab and outflow is observed between 4.5 and the mean low-tide elevation (8 mab). (b) average along-channel flood (dashed) and ebb profiles (solid) at C; asterisks mark ebb values at E and W and circles mark flood values at E and W. Nearly uniform shear over depth characterizes ebb whereas during flood the shear is concentrated near the bed. The discrepancy between the moorings on flood is further evidence of a flow disturbance at C on flood. (c) average cross-channel flood and ebb profiles at C where the symbols are as in the center panel.

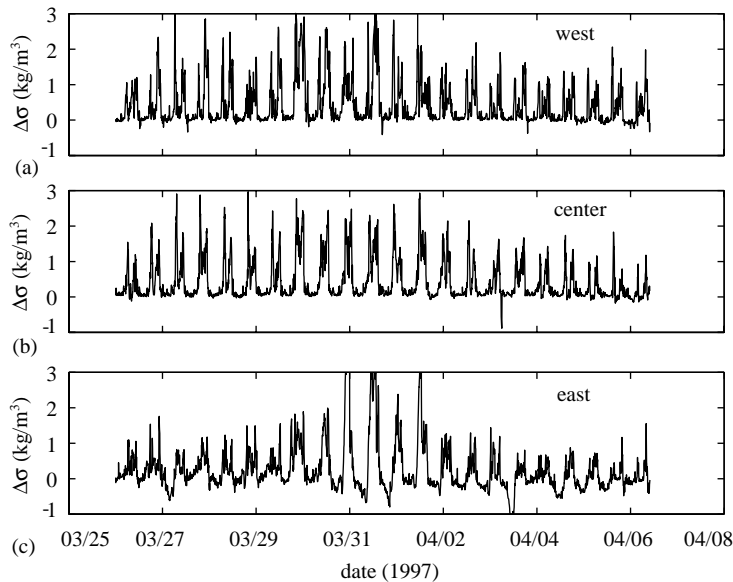


Fig. 7. Vertical density difference at west (a), center (b) and east moorings (c) demonstrates an abrupt transition between unstratified conditions on flood to stratified flow on ebb. The lower salinity sensor on the east mooring was malfunctioning intermittently and is shown for qualitative comparison.

A comparison of the density records at each of the moorings reveals that there is an abrupt transition in vertical stratification between flood and ebb. At all the moorings $1\text{--}3 \text{ kg m}^{-3}$ density differences between 0.66 and 2.5 mab are established soon after the beginning of ebb currents (Fig. 7). Vertical density differences are greatest during neap tides and decrease as spring tides are

approached near the end of the record. Stratification is established first at W about an hour after the change in tide, and at C about 1 h later. Given an along-channel separation of 1.5 km, this implies stratified fluid is advected along-channel at roughly 35 cm s^{-1} , consistent with observed flows. Stratification on ebb may also result from tidal straining (Simpson et al., 1990) but the abrupt

transition and sequential onset of stratification along the channel favor advection of lighter water from another region (possibly the large tidal creek just west of the shaded region in Fig. 2). Details of the stratification at E cannot be assessed because of the malfunctioning sensor but it appears to follow the same trends.

3.3. Direct stress estimates

Log-layer fits to the combined BASS/ADCP are of low quality on ebb (15% of the fits had $r^2 > 0.95$), and not meaningful on flood because of the flow distortion. They are not discussed further.

Direct estimates of the Reynolds stress $\langle -u'w' \rangle$ with BASS from the lowest 2 sensors are comparable, implying the existence of a nearly constant stress layer (Fig. 8), and consistent with an upward flux of momentum deficit on both phases of the tide. Values vary by a factor of four during ebb tide, increasing steadily between neap tide at the end of March and the end of the record. Flood tide values are considerably more erratic but show a qualitatively similar trend. Because of concerns about flow interference on flood we use only the ebb values in further analysis.

An estimate of the drag coefficient C_d is made by regressing $\langle -u'w' \rangle$ against u at 1 mab on ebb. There is considerable scatter in the relationship (Fig. 9), the squared correlation coefficient being 0.7. The average value of $C_d = 0.0017$, but it is obvious that a number of the highest stress estimates are not well represented by this regres-

sion. The values shown by asterisks were collected over the last two tidal cycles as the flow built towards its greatest values and when the stratification on ebb began to break down. The gradient Richardson number $Ri = -(g/\rho)(\partial\rho/\partial x/(\partial u/\partial x)^2)$, evaluated between 2.5 and 0.66 mab, was consistently above 0.25 during ebb for most of the deployment period but was beginning to drop below 0.25 on ebb near the end of the record (Fig. 10a). A comparison of the measured ebb velocity with $\langle -u'w' \rangle / C_d$ (Fig. 10b) shows that C_d is too small near the end of the record. The value of C_d for this last part of the record, fit to the values shown by asterisks, is 0.0025, plotted as the upper curve on Fig. 9 (with $r^2 = 0.88$), and a fit to the rest of the observations yields a $C_d = 0.0015$, shown as the lower curve ($r^2 = 0.78$).

We then estimate the bed stress τ_b as $C_d(u) * \max(u_{1m})^2 * \text{sign}(u_{1m})$. To account for the observed variability in C_d , when $u_{1m}^2 < 0.4 \text{ m}^2 \text{ s}^{-2}$ we use $C_d = 0.0015$ and when $u_{1m}^2 > 0.4 \text{ m}^2 \text{ s}^{-2}$ we use $C_d = 0.0025$. The maximum value of the current at 1 mab observed over the moored array is used for two reasons. First, it is used in place of the value at C because of the flow disturbance problem. Second, and more importantly, we expect the mean value of the stress on the bend to be determined largely by the maximum current speeds observed spatially, because the stress is proportional to u^2 .

Consistency of the observations with law of the wall behavior can be assessed by comparing the scaled shear $\kappa z \partial u / \partial z$ and bottom stress $\sqrt{\langle -u'w' \rangle} \text{sgn}(\langle -u'w' \rangle)$ (Trowbridge et al.,

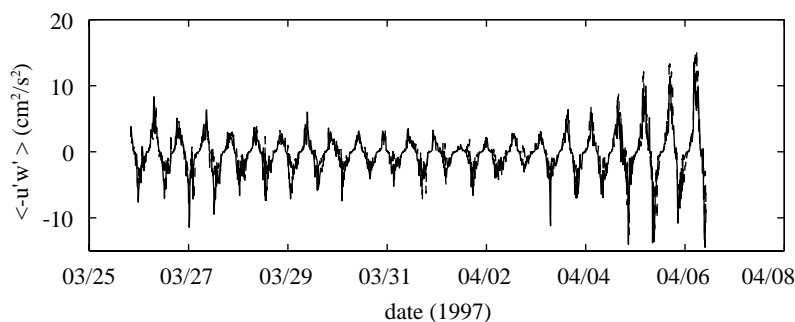


Fig. 8. Reynolds stress measurements from 0.28 to 0.67 mab at C; positive values occur during ebb. The values are consistent over time and in the vertical and show a strong neap-spring modulation.

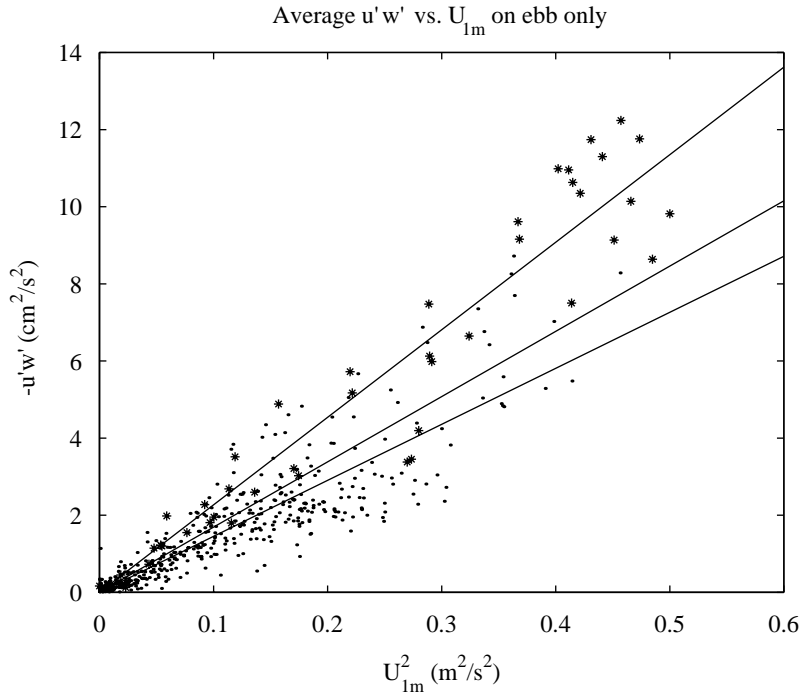


Fig. 9. Vertically-averaged Reynolds stress ($-u'w'$) is plotted as a function of velocity at 1 mab squared during ebb. Overlaid are regressions for the entire data set and selected times, yielding drag coefficient estimates of 0.0015–0.0025 (see text).

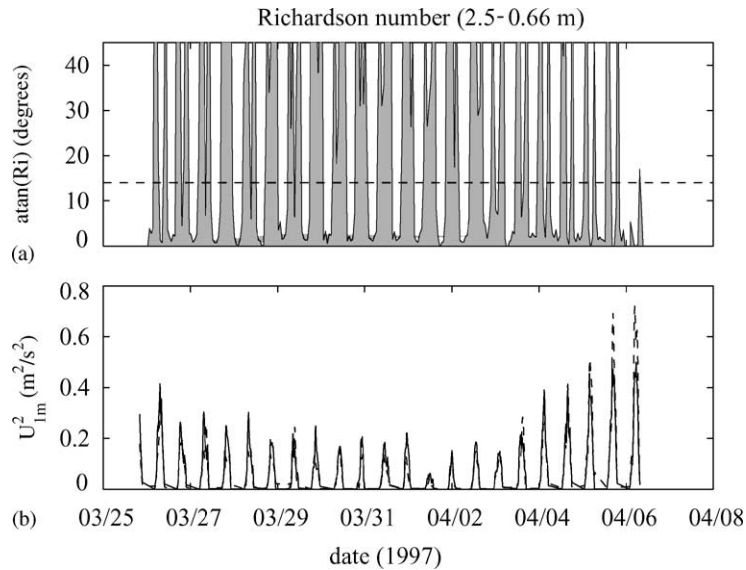


Fig. 10. (a) Gradient Richardson number between 2.5 and 0.66 mab, plotted as the arctangent. Ri exceeds 0.25 (dashed line) throughout ebb around the period of neap tide but is falling below 0.25 on ebb as the maximum spring tide approaches. (b) Comparison during ebb tide only of maximum along-channel velocity squared at 1 mab (solid line) and $\langle -u'w' \rangle / C_d$ (dashed line) where $C_d = 0.0015$. The comparison is favorable except for the last few tidal cycles when C_d is apparently too small.

1999). We use hour-averaged data and the shear formed using the lowest 3 sensors on BASS. The non-dimensional shear ϕ_m , the ratio of the scaled shear to bottom stress, should equal one if the boundary layer follows law of the wall behavior. Plots of the scaled shear versus the bottom stress (Fig. 11) during ebb are reasonably linear ($r^2 = 0.86$ – 0.89), consistently greater than one, and display a marked change in ϕ_m between neap (Fig. 11a) and spring (Fig. 11c) tides. The large values of Ri during neap tides and tendency toward small values during spring tides suggests that the variations in ϕ_m may be due in part to variations in stratification within the boundary layer.

3.4. Momentum balance

The observations can be used to assess the along-channel momentum balance over the array. We can directly evaluate the depth-averaged momentum balance

$$\partial \bar{u} / \partial t + g \partial \eta / \partial x + gH / \rho (\partial \rho / \partial x) = -\tau_b / H_{eff}, \quad (1)$$

where \bar{u} is the depth-averaged velocity, η is the free surface, H is the water depth at C, ρ is density, τ_b is the bottom stress, and H_{eff} is the effective water depth (whose interpretation is discussed below). The pressure gradients are estimated from observations at E and W and \bar{u} is formed at C. The barotropic pressure gradient dominates (1) (Fig. 12a), the local acceleration is roughly half as large, and the baroclinic pressure gradient term is a tenth of the barotropic term. The magnitude of the terms fluctuate between March 26 and early

April, reflecting subtidal water level variations. An obvious minimum is reached on April 2 after which the barotropic pressure gradient and local acceleration terms increase rapidly, and the baroclinic pressure gradient decreases.

The Reynolds stress $\langle -u'w' \rangle$ is roughly half τ_b estimated using the maximum velocity at 1 mab along the channel (Fig. 12b); the difference is even greater during flood when the measured values are thought to be impacted by flow interference. Maximum values of τ_b reach $10 \text{ cm}^2 \text{ s}^{-2}$ on each flood tide but are $< 5 \text{ cm}^2 \text{ s}^{-2}$ on ebb between March 30 and April 3.

Plotting the sum of the left-hand side of (1) against τ_b reveals a reasonably linear relationship with $r^2 = 0.87$ (Fig. 13a). The slope of the relationship is an estimate of the effective depth H_{eff} and is 3.24 ± 0.07 m. Because the depth of the system is varied and includes extensive intertidal regions, it is not clear what depth should be used to scale the bottom stress. Using H_{eff} we can form the right-hand side of Eq. (1). The comparison of the sum of the left-hand side of Eq. (1) and the depth-scaled bottom stress is remarkably good (Fig. 12c), and suggests that this linear balance is a reasonable representation of the depth-averaged momentum dynamics in this reach.

4. Discussion and conclusions

A repeatable current and density structure on a channel bend was observed to vary slowly with the

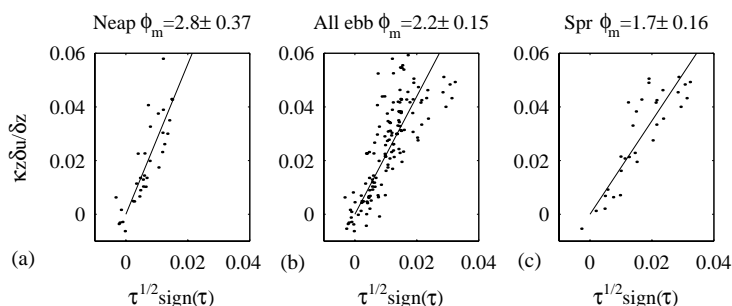


Fig. 11. Plots of the scaled shear versus bottom stress during ebb tides. The slope of the graphs is an estimate of the non-dimensional shear ϕ_m . Shown are conditions during neap tides (a), spring (c) tides, and all ebbs (b). Shear is enhanced relative to law of the wall behavior, especially during neap tides.

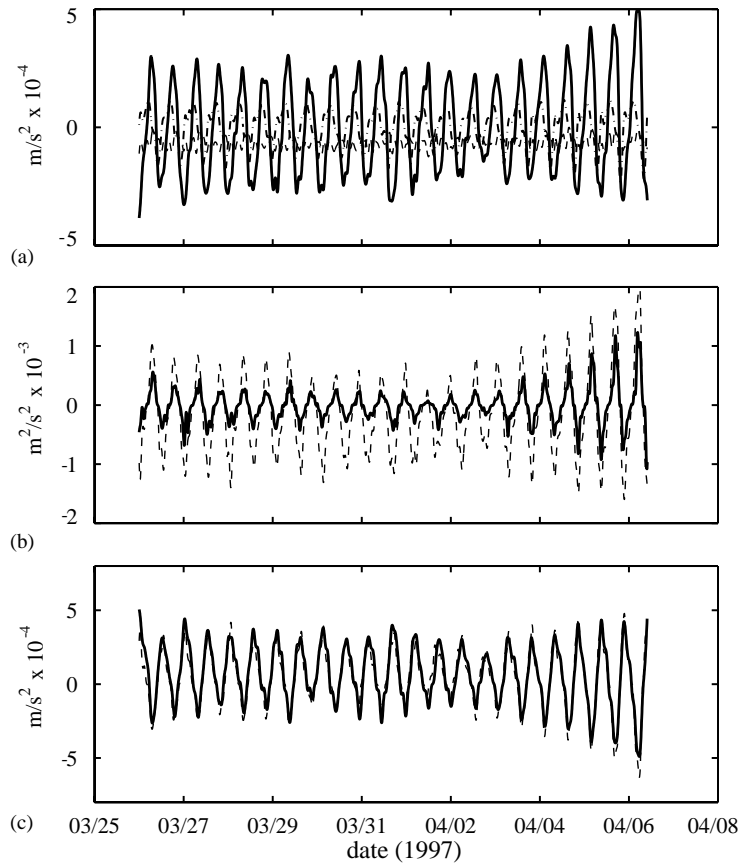


Fig. 12. (a) the barotropic pressure gradient (solid), baroclinic pressure gradient (dash) and local acceleration (dash-dot) terms as a function of time; b) a comparison of the measured stress $-u'w'$ (solid) and estimated (dash) bottom stress τ_b ; c) sum of local acceleration and pressure gradients (solid) and τ_b/H_{eff} (dashed).

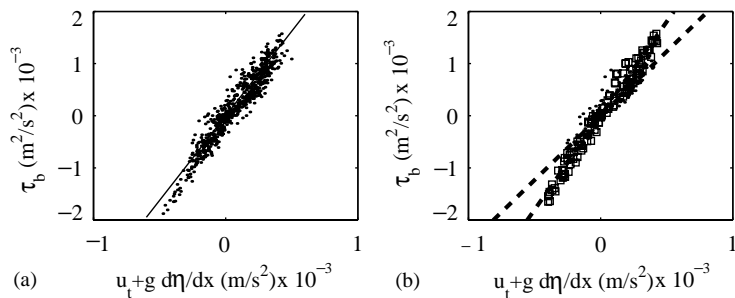


Fig. 13. Bottom stress versus the sum of local acceleration and pressure gradients for (a) the entire dataset and (b) 2-day periods near neap (asterisks) and spring (squares) tide. The slope of the linear fit is an estimate of the effective depth and is $H_{eff} = 3.2$ m for the full dataset, but varies between 2.5 ± 0.2 at neap tide and 3.6 ± 0.12 at spring tide.

spring-neap cycle. We interpret these features to result from a secondary circulation associated with the channel bend, the strength of which is

modulated over the spring-neap cycle. It consists of a helical flow moving toward the outside of the bend on the surface, downward at the outside of

the bend, and toward the inside of the bend near the bottom. This flow will carry high momentum near-surface fluid toward the bed as the flow moves through the bend, providing an explanation for the high velocities on the downstream end of the bend seen on spring tides. The unusual bathymetry on the bend of a nearly vertical outside wall may play an important role in this process. Because the channel is deepest at the outside of the bend, maximum velocities will develop there. A water parcel will experience only lateral friction on its descent down the vertical wall, and need only travel 10s of meters away from the wall before encountering the bottom of the channel and the current meters.

We can estimate the spatial scales of the helical flow as follows. The cross-channel velocity is roughly 5 cm s^{-1} (Fig. 6) at mooring C, $< 100 \text{ m}$ from the channel wall (Fig. 2). Given that the channel is about 8 m deep, continuity in the cross-channel direction suggests the vertical velocity at the outside bend should be $w = -dz * dv/dy = 8 * 0.05/100 = -0.004 \text{ m s}^{-1}$. Where the measurements were made the main channel is divided in two by a marsh island. The appropriate channel width is approximately 400 m . A water parcel starting at the surface near mid-channel would take $200/0.05 + 8/0.004 = 4000 + 2000 \text{ s}$ to reach the bottom. Assuming an average along-channel speed of 0.5 m s^{-1} the parcel completes this motion over 3 km , roughly the separation between the W and E moorings. This calculation is very sensitive to the magnitude of the vertical velocity, but a vertical speed of 1 cm s^{-1} seems quite reasonable for this very energetic system. Thus we expect that a water parcel can execute half of a circuit about the helix in traversing the channel bend.

Observations near spring tide of maximum velocities 1 mab at the most down-stream mooring are consistent with this helical flow carrying high momentum fluid from the surface to near the bed (Seim and Gregg, 1997). On ebb, the along-channel salinity gradient goes to zero, either because the densest fluid is advected onto the shoals on the inside of the bend by the helical flow or because the overturning motion mixes away the alongchannel structure. It is important to note that

both effects most strongly impact the seaward (downstream) end of the bend. On ebb, when this is in the same direction as the along-channel density gradient, this tends to reduce the near bottom along-channel density gradient. On flood, the helical flow most strongly impacts the landward end of the bend, tending to enhance the bottom along-channel density gradient.

At neap tide, currents were weaker and more variable, and the along-channel salinity gradient was maintained throughout the tidal cycle. Presumably this indicates that the helical flow is not established, consistent with the scaling arguments of Seim and Gregg (1997). They suggest that the cross-channel density gradient can be strong enough to suppress the helical flow, or possibly trap it in the upper water column. This requires raising the pycnocline on the inside of the bend and depressing it on the outside of the bend. A lack of the helical flow would explain why maximum currents no longer occur at the most downstream mooring at neap tides. When the current stops and reverses direction at low water, there is characteristically an abrupt increase in salinity, especially at the lowest sensors, followed by a series of wave-like variations (Figs. 5b and c). This low tide salinity increase is interpreted to result from the pycnocline tilt relaxing as the flow speeds go to zero, and the wave-like variations to reflect cross-channel seiching of the pycnocline.

Stratification in the lower few meters of the water column was strong enough to consistently raise the gradient Richardson number well above 0.25 over most of the ebb phase. Non-dimensional shear increased to values above 2 . Though other factors may also be responsible for enhancing the shear in the bottom boundary, in particular its limited height (Trowbridge et al., 1999), the variations in stratification explain some of the shear variability.

We find that the bottom stress during ebb tide is more variable over the spring-neap cycle than the bottom stress during flood tide. Similar results have been observed in the Hudson River (Peters and Bokhorst, 2000). The pronounced fortnightly sensitivity of stress and stratification during only one phase of the tide will likely have a large impact on the net flux of salt and sediment

and be important in long-term budgets of the estuary.

When the maximum current values in the mooring array are used to estimate bottom stress it roughly doubles the observed bottom stress. Part of the increase results from flow disturbance at the C mooring but systematic variation in flows along the channel were equally important. The reasonable momentum closure achieved when the maximum current is used suggests that the flow speed variability is an essential component of the dynamics that must be captured. Trowbridge et al. (1999) suggested that secondary circulation may be a process they did not capture in their observations that may be necessary to resolve to achieve a momentum balance. The secondary circulation associated with the channel bend is interpreted to be one of the major causes of the along-channel structure, implying that it is of fundamental importance in the momentum dynamics. It is reassuring that a simple drag law formulation and closely spaced moorings were sufficient to achieve a reasonable closure.

Our use of an effective depth permitted closure of the momentum balance; if the depth at C were used the bottom stress would be a factor of 2–3 too small. We feel its use is justified in this case because the depth in the system is so varied, and the surface slope, which is the principal forcing of the flow, is balanced by the friction experienced across the channel. The slope in this sense integrates the forces experienced by the flow. The effective depth is a weighting of areas (depths) that are most important in producing stress. Interestingly, the effective depth varies significantly between the neap and spring tide periods (Fig. 13b), being least at neap tides (2.47 ± 0.2 m) and greatest at spring tides (3.61 ± 0.12 m). The increased effective depth is consistent with the generation of enhanced shear stress by cross-channel mixing at spring tides. This implies the channels may account for a greater fraction of the total stress at spring tides when stratification is weakest.

Not only does the effective depth variously weight the areas in the estuarine system that produce stress, it may reflect other processes that alter the momentum balance, such as form drag. The marshes inside and outside the channel

boundaries play a role in the momentum balance that is far from clear. Some authors (e.g. Freidrichs et al., 1992) assume that intertidal areas act as mass sinks but do not play an important role in the momentum balance. Others (e.g. Kuo and Park, 1995) postulate that intertidal areas act as momentum sinks. Any large-enough mass sink or momentum sink alters the momentum balance, so the effective depth may further reflect the effect of intertidal areas on the vertically averaged momentum balance.

Acknowledgements

We gratefully acknowledge the following agencies who supported the work described in this paper: the Georgia Coastal Zone Management Program (Grant No. RR100-279/9262764), National Science Foundation Land-Margin Ecosystem Research (Grant No. DEB-9412089) and the State of Georgia through a water resources research grant to the Skidaway Institute of Oceanography.

References

- Blanton, J.O., Lin, G., Elston, S., 2002. Tidal current asymmetry in shallow estuaries and tidal creeks. *Continental Shelf Research* 22, 1731–1743.
- Cheng, R.T., 1988. Eulerian and Lagrangian model of estuarine hydrodynamics. In: Kjerfve, B. (Ed.), *Estuarine Hydrodynamics*, Vol. 1, CRC Press, Boca Raton, FL, pp. 149–159.
- Freidrichs, C.T., Lynch, D.R., Aubrey, D.G., 1992. Velocity asymmetries in frictionally-dominated tidal embayments: longitudinal and lateral variability. In: Prandle, D. (Ed.), *Dynamics and Exchanges in Estuaries and the Coastal Zone*. American Geophysical Union, pp. 277–312.
- Geyer, W.R., Trowbridge, J.H., Bowen, M.M., 2000. The dynamics of a partially mixed estuary. *Journal of Physical Oceanography* 30, 2035–2048.
- Hansen, D.V., Rattray Jr., M., 1965. Gravitational circulation in straits and estuaries. *Journal of Marine Research* 23, 104–122.
- Jay, D.A., Smith, J.D., 1990. Residual circulation in shallow estuaries, 2: weakly stratified and partially mixed, narrow estuaries. *Journal of Geophysical Research* 95, 733–748.

- Kjerfve, B., Seim, H.E., 1984. Construction of net isopleth plots in cross-sections of tidal estuaries. *Journal of Marine Research* 42, 503–508.
- Kuo, A.Y., Park, K., 1995. A framework for coupling shoals and shallow embayments with main channels in numerical modeling of coastal plain estuaries. *Estuaries* 18, 341–350.
- Peters, H., 1999. Spatial and temporal variability of turbulent mixing in an estuary. *Journal of Marine Research* 57, 805–845.
- Peters, H., Bokhorst, R., 2000. Microstructure observations of turbulent mixing in a partially mixed estuary, Part I: dissipation rate. *Journal of Physical Oceanography* 30, 1232–1244.
- Seim, H.E., Gregg, M.C., 1997. The importance of aspiration and channel curvature in producing strong vertical mixing over a sill. *Journal of Geophysical Research* 102, 3451–3472.
- Simpson, J.H., Brown, J., Matthews, J., Allen, G., 1990. Tidal straining, density currents, and stirring in the control of estuarine circulation. *Estuaries* 13, 125–132.
- Trowbridge, J.H., Geyer, W.R., Bowen, M.M., Williams III, A.J., 1999. Near-bottom turbulence measurements in a partially mixed estuary: turbulent energy balance, velocity structure and along-channel momentum balance. *Journal of Physical Oceanography* 29, 3056–3072.
- UNESCO, 1985. The international system of units (SI) in oceanography. UNESCO Technical Papers No. 45, IAPSO Pub Sci. No. 32, Paris, France.
- Williams, A.J., Tochko, J.S., Keohler, R.L., Grant, W.D., Gross, T.F., Dunn, C.V.R., 1987. Measurement of turbulence in the oceanic bottom boundary layer with an acoustic current meter array. *Journal of Atmospheric and Oceanic Technology* 4, 312–327.